

MTL TR 89-89

DTIC FILE COPY

AD

2

# A PROPOSED UNIAXIAL COMPRESSION TEST FOR HIGH STRENGTH CERAMICS

AD-A231 700

WILLIAM A. DUNLAY  
CERAMICS RESEARCH BRANCH

CARL A. TRACY  
MATERIALS DYNAMICS BRANCH

PAUL J. PERRONE  
MECHANICS AND STRUCTURES BRANCH

DTIC  
ELECTE  
FEB 08 1991  
S B D

September 1989

Approved for public release; distribution unlimited.



US ARMY  
LABORATORY COMMAND  
MATERIALS TECHNOLOGY LABORATORY



U.S. ARMY MATERIALS TECHNOLOGY LABORATORY  
Watertown, Massachusetts 02172-0001

91 2 07 017

The findings in this report are not to be construed as an official Department of the Army position, unless so designated by other authorized documents.

Mention of any trade names or manufacturers in this report shall not be construed as advertising nor as an official indorsement or approval of such products or companies by the United States Government.

#### DISPOSITION INSTRUCTIONS

Destroy this report when it is no longer needed.  
Do not return it to the originator.

UNCLASSIFIED

SECURITY CLASSIFICATION OF THIS PAGE (When Data Entered)

REPORT DOCUMENTATION PAGE		READ INSTRUCTIONS BEFORE COMPLETING FORM
1. REPORT NUMBER MTL TR 89-89	2. GOVT ACCESSION NO.	3. RECIPIENT'S CATALOG NUMBER
4. TITLE (and Subtitle)  A PROPOSED UNIAXIAL COMPRESSION TEST FOR HIGH STRENGTH CERAMICS		5. TYPE OF REPORT & PERIOD COVERED  Final Report
7. AUTHOR(s)  William A. Dunlay, Carl A. Tracy, and Paul J. Perrone		6. PERFORMING ORG. REPORT NUMBER
9. PERFORMING ORGANIZATION NAME AND ADDRESS  U.S. Army Materials Technology Laboratory Watertown, Massachusetts 02172-0001 SLCMT-EMC		8. CONTRACT OR GRANT NUMBER(s)
11. CONTROLLING OFFICE NAME AND ADDRESS  U.S. Army Laboratory Command 2800 Powder Mill Road Adelphi, Maryland 20783-1145		10. PROGRAM ELEMENT, PROJECT, TASK AREA & WORK UNIT NUMBERS  D/A Project: 1L1612105.H84
14. MONITORING AGENCY NAME & ADDRESS (if different from Controlling Office)		12. REPORT DATE  September 1989
		13. NUMBER OF PAGES  29
		15. SECURITY CLASS (of this report)  Unclassified
16. DISTRIBUTION STATEMENT (of this Report)  Approved for public release; distribution unlimited.		15a. DECLASSIFICATION/DOWNGRADING SCHEDULE
17. DISTRIBUTION STATEMENT (of the abstract entered in Block 20, if different from Report)		
18. SUPPLEMENTARY NOTES  Presented at the annual meeting of Amer. Ceram. Soc., April 25, 1989.		
19. KEY WORDS (Continue on reverse side if necessary and identify by block number)  Advanced ceramics Compression testing Finite element analysis Ceramics		
20. ABSTRACT (Continue on reverse side if necessary and identify by block number)  (SEE REVERSE SIDE)		

DD FORM 1 JAN 73 1473

EDITION OF 1 NOV 65 IS OBSOLETE

UNCLASSIFIED

SECURITY CLASSIFICATION OF THIS PAGE (When Data Entered)

Block No. 20

## ABSTRACT

Compressive strength is critical to the performance of ceramics in armor, machine tool bits, and compressively loaded structural components. Traditional compression tests yield misleadingly low values for high strength ceramics. A new test, utilizing a dumbbell-shaped specimen, has been developed and has successfully measured the strength of  $\text{Al}_2\text{O}_3$ ,  $\text{B}_4\text{C}$ ,  $\text{TiB}_2$ , and  $\text{SiC}$ . Compression strengths approaching 7 GPa (1 million psi) were measured. Results were accurate, reproducible, and consistent with present compressive fracture theory. A finite element analysis (FEA) was done to confirm a uniaxial stress state. An error analysis examines the severity of procedural errors. The test is simple and cost effective to perform.

# CONTENTS

	Page
INTRODUCTION .....	1
EXPERIMENTAL APPARATUS AND PROCEDURE	
Compression Specimens and Loading Blocks .....	2
Test Setup .....	4
Testing Procedure .....	4
RESULTS	
Compression Test Results .....	5
Finite Element Analysis .....	8
ERROR ANALYSIS	
Errors That Cause Failure to Initiate Outside the Gage Section .....	11
Loading Block Size Mismatch .....	11
Loading Block Compliance Mismatch .....	12
Irregular Loading Surfaces .....	12
Errors That Cause Erroneous Calculations of the Failure Stress Within the Gage Section ..	12
Errors in Theory .....	12
Eccentric Loading .....	13
Misalignment of Loading Blocks or Nonplanar Contacting Surfaces .....	13
Nonparallel Surfaces .....	15
Error Due to Measurement of Diameter of Gage Section .....	16
Error in the Load Measurement .....	16
CONCLUSIONS .....	16
APPENDIX A .....	18
APPENDIX B .....	22



<b>Accession For</b>	
NTIS GRA&I	<input checked="checked" type="checkbox"/>
DTIC TAB	<input type="checkbox"/>
Unannounced	<input type="checkbox"/>
Justification	
By _____	
Distribution/	
<b>Availability Codes</b>	
Dist	Avail and/or Special
A-1	

## INTRODUCTION

The purpose of this report is to present a uniaxial compressive strength test for advanced ceramics. It will be shown that the test procedure is accurate and reproducible, and is simple and cost effective as well.

The intended application of uniaxial compressive strength data presented in this report is primarily for research and characterization purposes. On the other hand compressive strength plays an important role in the performance of the component include ceramic armor, machine tool bits, and bioceramic body parts. Uniaxial compressive strength is a necessity in the design of these and other compressively loaded structural components.

Compressive fracture theory in brittle ceramics predicts that compressive strength should be reproducible and invariant with specimen size.<sup>1</sup> In contrast, the tensile strength of ceramics, due to its dependence on the statistical distribution of critical flaws, is known to vary with specimen volume or surface area. Therefore, a detailed statistical analysis is necessary before the tensile strength of a structure can be accurately characterized. As a result of the different fracture mechanisms involved, ceramics are frequently an order of magnitude stronger in compression than in tension. Compressive fracture is the result of a coalescence of many microcracks that grow and arrest under compressive loading.<sup>1</sup> When the density of microcracks reaches a critical point, structural integrity is lost and catastrophic collapse ensues. The origin of the microcracks may be microplasticity in the form of twinning,<sup>2</sup> or existing flaws such as pores and cracks or grain boundaries. Providing that the specimen size is much greater than the grain size or other microstructural scale, the compressive strength will be generally independent of volume.

The basic objectives in the design of the specimen and load-train configuration were to insure a valid uniaxial compressive failure and to minimize error and machining costs.<sup>3</sup> The load-train (Figure 1) consists of a dumbbell-shaped ceramic test specimen and tungsten carbide loading blocks. The specimen is loaded in a universal test machine fitted with hardened precision steel compressive fixtures. The geometry of the specimen was designed to insure compressive fracture in the reduced diameter gage section and to minimize any stress concentrations at the specimen fillets. The end caps are designed to allow for accurate alignment with the load blocks so as to minimize eccentric (bending) loading and insure that fracture does not initiate at the specimen end cap. The length of the gage section was kept short to avoid buckling, but large enough to provide a reasonable sampling volume and uniform stress state. Overall specimen size is not critical, as evidenced by the successful use of two sizes in this report. Specimen size is dictated, however, by machine capacities and the volume of material from which specimens can be machined.

1. ADAMS, M., and SINES, G. *A Statistical Micromechanical Theory of the Compressive Strength of Brittle Materials*. J. Am. Ceram. Soc., v. 61, no. 3-4, 1978, p. 126-131.
2. LANKFORD, J. *Compressive Strength and Microplasticity of Polycrystalline Alumina*. J. Mat. Sci., v. 12, p. 791-796.
3. TRACY, C. *A Compression Test for High Strength Ceramics*. J. Testing and Evaluation, American Society for Testing and Materials, 1987, p. 14-19.

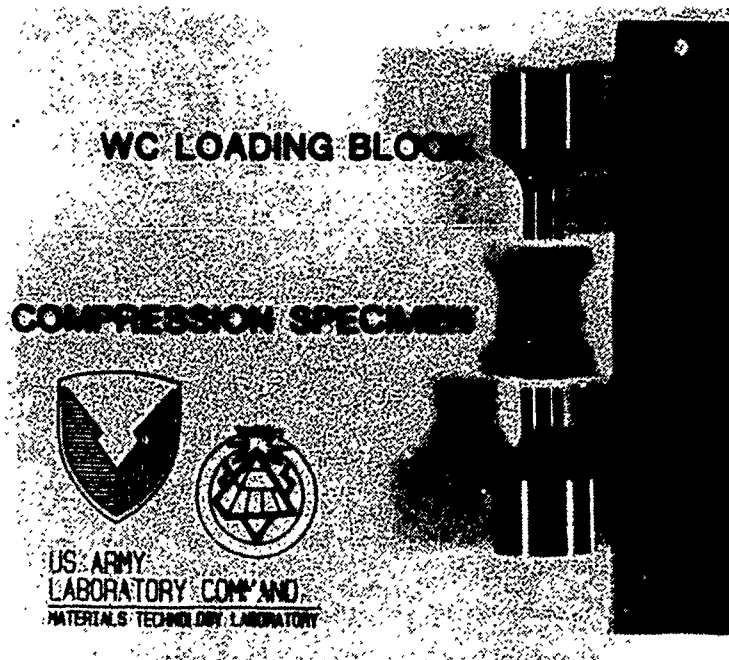


Figure 1. Ceramic uniaxial compression test specimen with tungsten carbide loading blocks.

## EXPERIMENTAL APPARATUS AND PROCEDURE

### Compression Specimens and Loading Blocks

Two uniaxial compression test specimen sizes, A and B, have been designed. Table 1 lists the important dimensions for each specimen size. Figure 2 illustrates the basic design of the specimen and labels the sections as they will be referred to in this report. Loading is in the axial direction. Expansion and bulging due to Poisson's effect occur in the lateral direction. Detailed drawings of the specimens, as well as the corresponding loading blocks including dimensions and tolerances, are presented in Appendix A. The selection of proper specimen size is affected by the dimensions of the billet from which the specimens are to be machined but, more importantly, by the capacity of the testing machine. Size A was used for the first set of alumina specimens. For a second set of the same alumina, and for all other materials, size B was used. Loads as high as 130,000 N (30,000 lb) were required for some B-size specimens, which corresponds to 210,000 N (47,000 lb) for an A-size specimen. This load would have come uncomfortably close to the 220,000 N (50,000 lb) capacity of the load cell that was used, hence the use of the B specimens.

Of particular importance in the machining of specimens is the quality of fillet #1 (Figure 2). This fillet must smoothly blend at the tangency point with the gage section with a minimum of discontinuity in order to minimize stress concentration at that location. Fillet #2, being in an area of lower stress, is not as critical.

Table 1. SUMMARY OF SPECIMEN DIMENSIONS

Specimen Size	Total Length [cm (in.)]	Length Gage [cm (in.)]	Diameter Gage [cm (in.)]	Volume Gage [cm <sup>3</sup> (in. <sup>3</sup> )]	Diameter End Cap [cm (in.)]
A	3.65 (1.44)	0.953 (0.375)	0.635 (0.25)	0.302 (0.018)	1.27 (0.5)
B	3.05 (1.2)	0.762 (0.3)	0.508 (0.2)	0.150 (0.009)	1.02 (0.4)

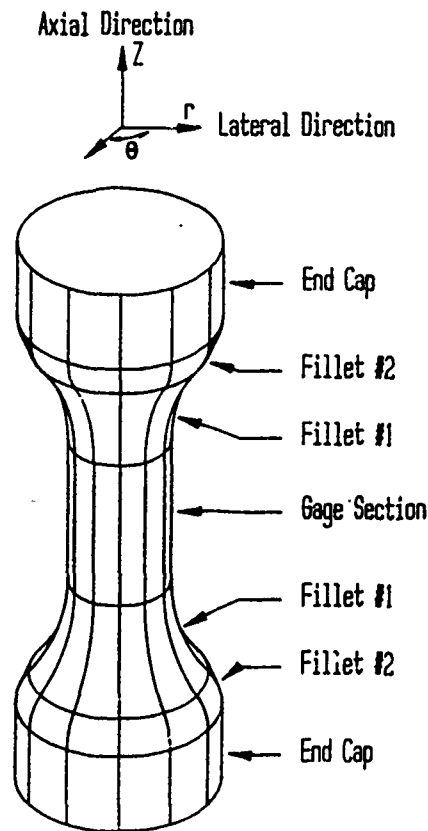


Figure 2. Compression test specimen.

The loading blocks were made from tungsten carbide\* (WC) with 7.8% cobalt binder. WC was chosen for its advantageous properties which include a high hardness, elastic modulus of 600 GPa, transverse rupture strength of 2.6 GPa, a stated compressive strength of 4.48 GPa, and machinability to ultraprecise tolerances; e.g., parallelism and perpendicularity to within 1.3  $\mu\text{m}$ . Because the WC loading blocks are less compliant than the ceramic compression specimens, they will exert a constraining effect on the specimen end caps by creating a relatively small biaxial compressive force in the lateral plane. This reduces the chance of end-cap failure during the test.

\*Kennametal, grade K3406.



## Test Setup

A universal testing machine<sup>†</sup> with a 220 kN (50,000 lb) capacity was used. Basic hardened steel compression fixtures were installed. A 30 x 30 x 2.5-cm polished steel compression table was bolted to the base of the machine while a compressive anvil with a face diameter of 13 cm and 5 cm thick was screwed into the load cell. Each fixture had a 2.54-cm-diameter (1 inch) concentric circle inscribed on its loading surface for visual alignment of the WC loading blocks. The compression table and the anvil themselves had to be aligned. This was accomplished by centering a 2.54-cm-diameter cylinder on the compression table, loading the cylinder lightly with the anvil, and checking to see that the cylinder was also aligned with the anvil. Adjustment was made by moving the compression table laterally within the tolerance provided by the holddown bolts.

The loading surfaces were then checked for parallelism. This was done only within the top and bottom 2.54-cm concentric circles since they are the only critical surfaces. The procedure was as follows. A dial gage was mounted against the lower surface of the anvil so that its position, with respect to the base of the testing machine, could be determined. The location of the gage is not critical. A 15 x 0.6 cm (the exact dimensions are not important) square-ended rod was then placed between the anvil and compression table so that the ends seated squarely on the loading surfaces and were visually centered within the inscribed circles. After loading the rod to 50 lb, the dial gage was zeroed and this center measurement became the reference. The parallelness of the surfaces was measured by loading the rod in the same manner at the 12, 3, 6, and 9 o'clock positions around the circle and recording the dial gage reading at each position. All readings should be within 10  $\mu\text{m}$  (0.0004 in.). The magnitude and direction of any nonparallelism was then determined and corrected for by adding shims underneath the compression table. In this case, it was necessary to shim the left side of the base 0.66 mm (0.026 in.). Note that because of the geometry of the base plate, a small adjustment within the inscribed circle required a much larger adjustment be made at the outer edge of the plate. Parallelism was checked in this manner frequently to insure that the successive loading cycles were not changing the alignment.

## Testing Procedure

The primary concern during testing was that the load-train components be parallel and concentric. Prior to each test, any nicks in the anvil or compression table were removed with emery cloth and all surfaces were cleaned with acetone. The alignment system (Figure 3) consisted primarily of a precision machinist's V-block, 4.5 cm in length. The V-block was used to align the specimen end caps with the corresponding section of the load blocks. The V-block was supported vertically by two 32-mm blocks and placed in the center of the compression table. The two load blocks and the specimen were then assembled and pushed into the V-block. The entire assembly, while being firmly held together, was then visually aligned with the 2.54-cm circle inscribed in the compression table. The crosshead was slowly lowered until a small preload was developed, and the alignment system was removed.

The degree of alignment was determined by drawing fine pencil lines, parallel to the axis of the specimen and extending across the specimen/loading block interfaces, at various points around the circumference. A very small step, or overhang, can be detected in this manner.

<sup>†</sup>Instron Corporation, Model 1127.

According to specifications, the load block should be slightly larger (0 to 30  $\mu\text{m}$ ) than the end cap, therefore, the alignment procedure was considered a success if the load block was flush or slightly overhanging the specimen at all points around the circumference. The alignment procedure was repeated as necessary.

Tape was used to prevent the WC fixtures and the larger pieces of the specimen from flying about after failure. A clear acrylic box was placed around the test assembly to contain the high velocity particles generated by the explosive failure of the specimen. Crosshead speed was 0.51 mm/min (0.02 in./min) and the chart speed was 5.1 cm/min (2 in./min). Initially, a preload of 1,800 N was used, but this was later changed in favor of a 9,000 N preload because the loading rate below 9,000 N was very slow.

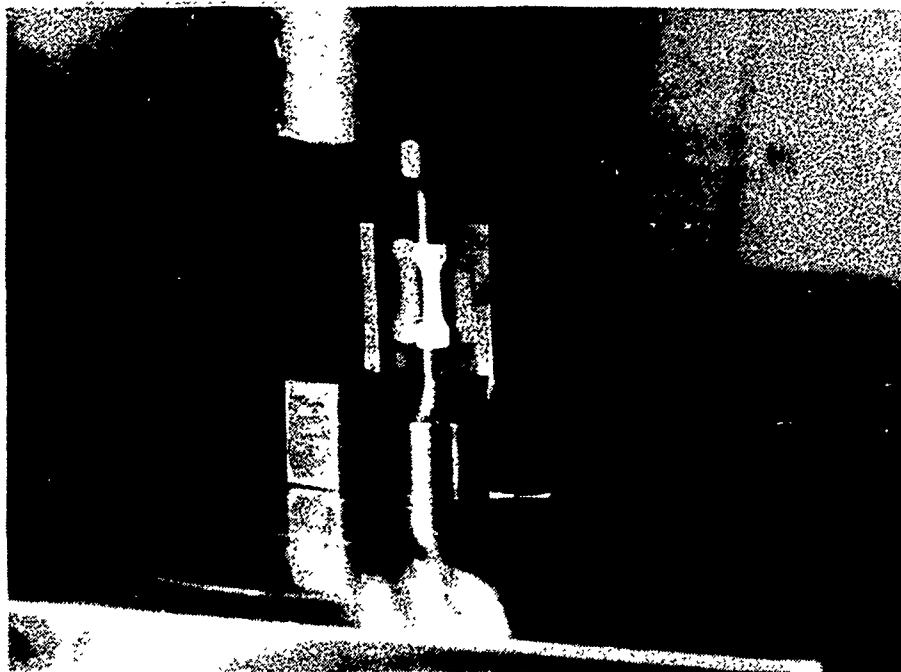


Figure 3. Specimen and loading blocks aligned with machinist V-block and installed in test machine's hardened steel fixtures.

After each test, the debris was swept from the compression table and collected for further study. It was noted if the specimen end caps were intact or broken and if the load blocks were damaged in any way. Load blocks with even slight damage were not used for further testing since any irregularity could cause a stress concentration at the specimen - load block interface during the next test.

## RESULTS

### Compression Test Results

The typical compression test proceeded as follows. The load would rise slowly as the initial slack in the load train was taken up. At about 9,000 N (2,000 lb), the loading rate increased abruptly and continued to rise in a nearly linear fashion until failure. Failure was

an explosive event accompanied by a loud report and a flash of light (visible in a darkened-room). The gage section, and most of the tapered sections as well, was reduced to very fine rubble ranging in size from several millimeters to powder that took a good fraction of a minute to settle to the ground. The end caps were either left intact or were cracked into several pieces.

A total of seven materials were tested using the dumbbell-shaped uniaxial compression test. A summary of those materials is given in Table 2. Individual test results are given in Table 3. The numbers given as percents are the coefficient of variation (standard deviation divided by mean). Table 4 lists the materials tested in order of ascending compressive strength, together with other mechanical properties of the materials, as available from testing done at the U.S. Army Materials Technology Laboratory (MTL). Examining Table 4, it can be seen that compressive strength does not correlate well with other mechanical properties. This would indicate that compressive strength is an independent intrinsic material property and not simply a function of other more commonly measured properties such as elastic modulus, hardness, toughness, etc. It is interesting to note that the strongest material, the alumina with silicon carbide fibers, is far stronger than the sintered alumina.

Table 2. SUMMARY OF MATERIAL SPECIFICATIONS

Material	Source	Composition	Process	Density (g/cm <sup>3</sup> )	Tile & Vintage
Alumina Al <sub>2</sub> O <sub>3</sub>	Coors AD-94	94% Pure	Sintered	3.37	15 x 15 x 2.5 cm 1984
Tungsten Carbide WC	Kenne-metal Grade 3406	7.8% Co	Hot Pressed	14.7	1987
Boron Carbide B <sub>4</sub> C	Ceradyne	—	Hot Pressed	2.47	15 x 15 x 2.5 cm 1983
Alpha Silicon Carbide SiC-S	Carborundum Hexaloy	98.5% Pure	Sintered	3.12	15 x 30 x 2.5 cm 1985
Silicon Carbide SiC-HP	Norton NC-203	95% Pure	Hot Pressed	3.32	15 x 15 x 2.5 cm 1985
Titanium Diboride TiB <sub>2</sub>	Ceradyne Ceraloy #225	98.5% Pure	Hot Pressed	4.5	20 x 20 x 2.5 cm 1983
Alumina With Silicon Carbide Whiskers Al <sub>2</sub> O <sub>3</sub> /SiC	Arco	99% Pure Al <sub>2</sub> O <sub>3</sub> 25 wt% Whiskers	Hot Pressed	3.7	15 x 15 x 2.5 cm 1986

Table 3. UNIAXIAL COMPRESSION STRENGTH. INDIVIDUAL TEST DATA (GPa)  
PERCENT FIGURES ARE THE COEFFICIENT OF VARIATION

Test #	Al <sub>2</sub> O <sub>3</sub> Size A	Al <sub>2</sub> O <sub>3</sub> Size B	WC Size B	B <sub>4</sub> C Size B	SiC-S Size B	SiC-HP Size B	TiB <sub>2</sub> Size B	Al <sub>2</sub> O <sub>3</sub> /SiC Size B
1	3.51	3.56	4.28	4.88	5.24	6.65	5.33	5.62
2	3.42	3.59	4.29	3.73	4.53	6.16	5.65	6.10
3	3.40	3.68	4.30	5.13	4.74	6.11	5.65	6.74
4	3.43	3.80	—	5.13	4.67	6.02	5.84	6.54
5	3.45	3.56	—	4.83	4.14	5.92	5.43	6.55
6	3.56	3.60	—	4.67	4.07	6.20	5.86	6.54
7	3.61	3.61	—	4.49	5.08	6.36	5.84	6.67
8	3.49	3.44	—	5.43	4.57	6.79	5.63	6.55
9	3.44	3.41	—	4.43	4.61	6.36	5.87	6.55
10	3.63	3.70	—	4.49	3.87	6.32	5.65	6.08
Mean	3.49 ± 2%	3.59 ± 3%	4.29	4.83 ± 7%	4.55 ± 9%	6.29 ± 4%	5.67 ± 3%	6.40 ± 5%

Table 4. SUMMARY OF MECHANICAL PROPERTIES ARRANGED IN ORDER OF  
INCREASING COMPRESSION STRENGTH

Material	$\sigma_c$ (GPa)	$E^\dagger$ (GPa)	$\nu^\ddagger$	$\sigma_b^{**}$ (MPa)	Weibull <sup>o</sup> (M)	$H^{oo}$ (GPa)	$K_{Ic}^\#$ (MPa <sup>m</sup> <sup>1/2</sup> )
Al <sub>2</sub> O <sub>3</sub> Size A	3.49 ± 2%	280(231)	0.23	—	—	10.2	3.5 - 4.0
Size B	3.59 ± 3%	280(281)	0.23	—	—	10.2	—
WC	4.29	606	0.28	—	—	17.5	—
SiC-S	4.55 ± 9%	408	0.16	312 ± 11%	10.8	20.9	3.0
B <sub>4</sub> C	4.83 ± 7%	441	0.17	402 ± 21%	5.2	24	—
TiB <sub>2</sub>	5.67 ± 3%	550(600)	0.11	398 ± 4%	29	18	6.7
SiC-HP	6.29 ± 4%	445(484)	0.17	694 ± 11%	9.6	20	5.2
Al <sub>2</sub> O <sub>3</sub> /Si	6.40 ± 5%	392	0.22	451 ± 18%	5.1	15	7.3

\*Uniaxial compressive strength

†Elastic modulus sonic method (strain gage method)

‡Poisson's ratio sonic method

\*\*MIL-STD-1942(MR) size B, mean flexure strength ± coefficient of variation

o Weibull slope of the flexure strength data

oo Knoop hardness, 1,000 gf

#Critical stress intensity factor (double torsion test)

One concern that arose during the design of the two different size compression test specimens was the possibility of a size-dependent strength relationship. There is a decided volume or surface area strength dependence of brittle materials when subjected to tensile loading since failure occurs from the largest critical flaw. As specimen size increases, the size of the critical flaw will increase, therefore, the strength decreases. Failure due to compressive loading is fundamentally different in that it involves the generation and accumulation of large numbers of microcracks which

interact at some critical density to cause loss of structural integrity and ultimate collapse.<sup>1,4</sup> Therefore, compressive strength is not expected to have a volume dependence. As shown in Table 4, the compressive strength of the smaller B specimen is only 3% greater than the A specimen. This is still statistically significant considering the small standard deviation for each sample. Another FEA is underway to determine the stress concentration factor of the larger A specimen but considering the testing was performed by different investigators with an elapsed time of 3 years, the data is surprisingly consistent and reproducible.

It was originally felt that if the end caps of the compression specimen cracked during the test, the test should be considered invalid.<sup>3</sup> More recent data has shown this to be an improper test criteria. Any test in which failure initiates outside of the gage section, or in which any of the problems discussed in the Error Analysis Section is excessive, should be considered invalid. Initially, it was thought that a cracked end cap was an indication of this type of problem. However, broken end caps did not correlate with low compression strength for any of the materials and, for the size B alumina, breakage occurred only in three of the strongest four specimens. This would indicate that the end caps are failing due to tensile stress waves generated after initial failure; therefore, the stress measurement is not affected.

Most of the end-cap failures fell into two categories: (i) lateral cracks perpendicular to the specimen axis and (ii) axial cracks parallel to the axis. It is thought that the lateral cracks are produced by the propagating tensile wave generated by the almost instantaneous release of elastic strain energy within the specimen upon gage-section collapse. These cracks occur in material that is under enormous compressive load prior to the moment of failure in the gage section and, therefore, cannot be the initial site of failure and are not a reason for concern. The axial cracks, on the other hand, could conceivably be generated by radial or hoop tensile forces. A radial crack initiated in the end cap could propagate into the gage section, creating enough of an instability to initiate compressive failure at a load lower than the true compression strength. The data did not indicate that this was occurring, therefore, all data points were included.

One possible cause of end-cap failure is compliance mismatch between end cap and loading block (see the Loading Block Compliance Mismatch Section). If compliance mismatch was significant, it would follow that the materials with the more severe mismatch would have a higher rate of end-cap failure. No such correlation was found, indicating that for the seven materials tested, compliance mismatch was not a problem. Finite Element Analysis (FEA) reinforced this conclusion (see the Finite Element Analysis Section).

A number of specimens were strain gaged during the compression test. An elastic modulus was calculated from this strain measurement and the calculated stress value. These results are given in Table 4 in parentheses and show fairly good agreement with the sonic values.

### Finite Element Analysis

To evaluate the present specimen design as a true test of uniaxial compression strength, an FEA was performed. The purpose of the analysis was to determine: (i) if the gage-section stress state is actually one of uniaxial compression, (ii) what the maximum compression stress is and where it occurs, and (iii) if significant tensile stresses are generated anywhere in the specimen. The details of the analysis and the contour stress plots generated are included in Appendix B.

<sup>4</sup> MESCALL, J., and TRACY, C. *Improved Modeling of Fracture in Ceramic Armors*. Proceedings of the 1986 Army Science Conference, 1986.

The FEA reveals that the stress is essentially uniaxial in the gage section. Radial and hoop stresses are compressive and less than 1% of the axial stress. The maximum compressive principal stresses ( $\sigma_3$ ) are nearly identical to the axial stresses, indicating that the shear stress is not of significant magnitude. The axial stress, at  $z = 0$  (the midpoint of the specimen), is essentially constant across the gage section.

The maximum compressive stress occurs on the surface of the specimen where the gage section meets fillet #1 (Figure 4). Figure 5 shows the deformation (greatly exaggerated) of the compression specimen under load. One can get a physical appreciation for the stress concentration at the junction between fillet and gage section by noting the bending that occurs around this point. For alumina, the axial stress is 3.95 GPa and  $\sigma_3$  is 3.96 GPa at this point of stress concentration. These values are 9% higher than the nominal stress of 3.59 GPa, which represents the average stress across the gage cross section. It seems likely that the failure initiates within this region of concentrated stress and that nominal stress is a conservative estimate of the material strength.

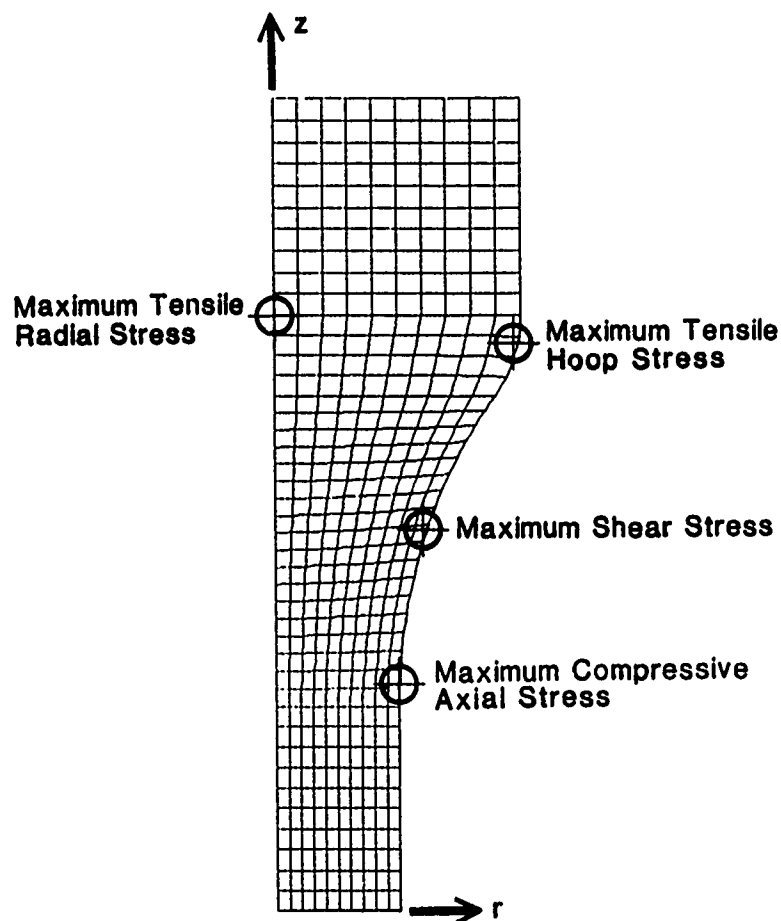


Figure 4. Finite element mesh (1/4 of actual specimen) showing the locations of maximum stresses.

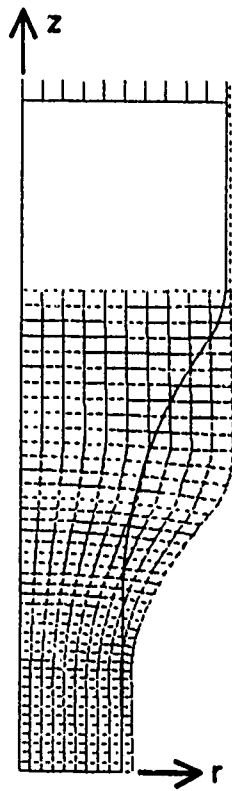


Figure 5. Deformation of the finite element mesh under load (displacement greatly exaggerated) shows the bending that occurs around the tangency point between fillet and gage section. Solid lines indicate initial configuration and dashed lines indicate the deformed configuration.

Both the radial ( $\sigma_r$ ) and hoop ( $\sigma_\theta$ ) components of stress are tensile in the specimen end caps. The region of maximum tensile radial stress, which reaches a value of 126 MPa in the alumina, is indicated in Figure 4 on the axial centerline. Along this centerline, the radial and hoop stresses are equal. The maximum tensile hoop stress is located on the exterior boundary on fillet #2 and is 213 MPa for alumina. The first principal stress ( $\sigma_1$ ) (maximum tensile) is dominated by the hoop stress in the entire end cap and, in fact, the respective maxima are identical. Table 5 summarizes the results for each material.

Although the tensile stresses generated in the end caps are, in all cases, less than the tensile strength, it may be possible for tensile failure to occur. Damage that accumulates due to the enormous axial compressive load could reduce the lateral strength of the material, allowing failure in a tensile mode. However, the maximum tensile stresses occur in areas of relatively low axial stress, so most of the tensile strength is probably maintained. It is felt that failure initiation due to tensile stresses has not occurred in the present study, since tensile stresses are less than tensile strengths and end cap failure has not correlated with low compression strengths.

Table 5. RESULTS OF FINITE ELEMENT ANALYSIS SHOW THAT THE MAXIMUM COMPRESSIVE AXIAL STRESS  $\sigma_z$  IS HIGHER THAN THE NOMINAL STRESS  $\sigma_c$  DUE TO A STRESS CONCENTRATION. PERCENT ERROR IS DEFINED AS:  $(\sigma_c - \sigma_z)/\sigma_z$ . THE MAXIMUM TENSILE STRESS IN EACH MATERIAL IS SHOWN COMPARED TO THE RESPECTIVE FLEXURE STRENGTH. THE MODEL WAS LOADED FOR EACH MATERIAL SO THAT THE NOMINAL STRESS IS EQUAL TO THE EXPERIMENTAL VALUE FROM TABLE 4.

Material	Compressive			Tensile		
	$\sigma_c$ (GPa)	$\sigma_z$ (GPa)	% Error	Hoop (MPa)	Radial (MPa)	Flexure Strength (MPa)
Al <sub>2</sub> O <sub>3</sub>	3.59	3.95	-9.1	213	126	—
WC	4.29	4.69	-8.5	281	150	—
SiC-S	4.55	5.00	-9.0	221	168	312
B <sub>4</sub> C	4.83	5.31	-9.0	241	177	402
TiB <sub>2</sub>	5.67	6.24	-9.1	230	217	398
SiC-HP	6.29	6.92	-9.1	314	232	694
Al <sub>2</sub> O <sub>3</sub> /SiC	6.40	7.03	-9.0	367	228	451

### ERROR ANALYSIS

There are a number of possible sources of error in performing the uniaxial compression strength test. These errors are of two basic types. The first category of errors are those which cause failure of the specimen outside of its gage section in material that is not in a uniaxial stress state. The second category includes errors in determining the actual failure stress at the point of failure in the gage section.

#### Errors That Cause Failure to Initiate Outside the Gage Section

During a successful compression test, the stress in the end caps due to the larger cross-sectional area, is considerably lower than the stress in the gage section. Therefore, as the load increases, failure will occur in the gage section as long as the material is of homogeneous strength. However, it is possible to create localized stresses at the loading block specimen interface that will cause failure of the end cap and, ultimately, the whole specimen, at a point during the test when the gage-section stress is considerably below the true compression strength of the sample. Because it is difficult during the post mortem to assess whether this kind of failure has occurred, it is necessary to minimize the possibility of premature end-cap failure.

#### Loading Block Size Mismatch

In order to have uniform distribution of the compressive load, the end cap and the loading block diameters must be the same size. If they are not, the abrupt change in diameter acts like a fillet of zero radius, resulting in a singular stress field. Therefore, either the edge of the specimen or the loading block will deform or fracture, possibly leading to stress concentrations in the remaining material that could cause failure of the specimen at a stress lower than its actual compressive strength.<sup>5</sup>

<sup>5</sup> SINES, G., and ADAMS, M. *Compression Testing of Ceramics* in *Fracture Mechanics of Ceramics*, Plenum Press, New York, v. 3, 1978, p. 403-434.



## Loading Block Compliance Mismatch

It is possible to create tensile stress across the face of the end cap if the loading block material is not chosen correctly. If the tensile stress is large enough, the end cap will split and cause premature failure of the specimen. Strain in the lateral direction ( $\epsilon$ ) for a material under a longitudinal compressive stress ( $\sigma$ ) is  $\epsilon = (\nu/E)\sigma$  for isotropic materials where  $\nu$  = Poisson's ratio,  $E$  = Young's modulus, and the quantity  $\nu/E$  is the compliance. If, under load, the lateral strain in the block is greater than in the specimen, a tensile splitting force will be generated in the end cap, causing it to fail if the tensile strength is exceeded. Yielding of the loading block would make matters worse. In this case, the plastic and elastic strains would combine to create a splitting effect in the end cap.<sup>5</sup>

The optimum arrangement is to have less strain in the loading block, creating a radial compressive force on the specimen surface. This would aid in maintaining the integrity of the end cap by compensating for any localized tensile forces that would be induced by irregularities in the opposing surfaces. Care should be taken that the tensile force that would result in the load block does not cause it to fail.<sup>5</sup>

## Irregular Loading Surfaces

Failure of the end cap may result from local stresses induced by irregularities in the mating surfaces between block and specimen. Some researchers have inserted a thin layer of various materials between the contacting surfaces in an effort to spread the load out evenly. These efforts have met with mixed success, sometimes drastically reducing the strength.<sup>5</sup> The best solution, apparently, is to have as perfect mating surfaces as possible in direct contact, this being accomplished by lapping the surfaces against each other<sup>5</sup> or, as in the present case, by calling for exceedingly close tolerances for flatness and parallelness.

## Errors That Cause Erroneous Calculations of the Failure Stress Within the Gage Section

Assuming that failure does initiate in the gage section as desired, there are several sources of error that will cause the actual failure stress at the point of initiation to be different than the nominal stress calculated for the gage section. The nominal stress ( $\sigma_c$ ) is given by  $\sigma_c = P/A$  where  $P$  = the applied uniaxial load and  $A$  is the cross-sectional area of the gage section. In the following analysis, the percent error (ERR) will be defined as:

$$ERR = 100[(\sigma_c - \sigma_x)/\sigma_x] \quad (1)$$

where  $\sigma_x$  is the actual stress (allowing for the particular source of error that is being discussed). Thus, a positive error indicates  $\sigma_c$  overestimates the true stress, while a negative error indicates that  $\sigma_c$  is an underestimate.

## Errors in Theory

In theory, the stress everywhere in the gage section of a properly loaded specimen is simply the nominal stress  $P/A$ . The stress elsewhere in the specimen is lower because the cross-section area is greater. This requires two assumptions that are not necessarily true. The first is that there are no stress concentrations in or immediately adjacent to the gage section, because these would necessarily raise the local stress above the nominal value. Further, there must be no stress concentrations in the end caps of sufficient magnitude to create a local zone of stress greater than the gage-section stress. Finite element analysis has shown that,

for the specimen shape used in the present report, there is a region of stress concentration approximately 9% higher than nominal (see the Finite Element Analysis Section) at the transition from the gage section to fillet #1.

The second assumption is that the material in question is homogeneous in structure and, particularly, in its mechanical properties. If it is not, the stress will vary throughout the specimen and the nominal stress will represent an average value.

### **Eccentric Loading**

Eccentric loading occurs whenever the compressive load is not applied symmetrically around the center line of the specimen. This can occur for a number of reasons, the most obvious of which is if the loading blocks and specimen are not aligned properly. Eccentricity can also occur if the contacting surfaces are not smooth, planar, and parallel. The difficulty with an eccentric load is that it introduces a bending moment into the specimen with the resultant compressive and tensile loads being superimposed onto the uniaxial compressive stress. Eccentric loading is analyzed in two ways. For misalignment of the load blocks or nonplanar contacting surfaces, the load is assumed to be applied at a distance  $e_r$  from the center line of the specimen. For nonparallel surfaces, a misalignment angle ( $\theta$ ) is assumed.

### **Misalignment of Loading Blocks or Nonplanar Contacting Surfaces**

An area load that is not symmetric around the specimen axis can be modeled as a point load applied at a distance  $e_r$  away from the axis (Figure 6a). This load, in turn, is equivalent to a point load at the axis plus an applied moment  $M$  (Figure 6b). The moment  $M$  is given by  $M = P(e_r)$ . Simple beam formulations show that the maximum stress due to bending ( $\sigma_b$ ) is located on the surface of the specimen and is given by:

$$\sigma_b = \pm 4Pe_r/(\pi r^3).$$

The actual stress is then:

$$\sigma_x = \sigma_c(1 \pm 4e_r/r). \quad (2)$$

The error on the inside of the bend ( $\sigma_b$  is compressive) is:

$$\text{ERR} = (100)(-4e_r)/(4e_r + r). \quad (3)$$

The above analysis is oversimplified in that it does not take into account a second moment generated by the bending of the specimen. As the specimen bends (initially because of the eccentric load) its central axis moves a distance  $y$  laterally. A new moment,  $M = Py$ , develops because the specimen axis is no longer straight. Allowing for this effect, the stress in the gage section is given by:<sup>6</sup>

$$\sigma_x = \sigma_c \{1 \pm (e_r/r_g^2) \sec[(P/EI)^{1/2}(L_c/2)]\} \quad (4)$$

6. BEER, F., and JOHNSTON, E. R. Mechanics of Materials, McGraw-Hill, New York, 1981, p. 396-401, 544.

where  $r_g$  = the radius of gyration,  $I$  = the moment of inertia, and  $L_e$  = the effective length of the column (gage section). For the cylindrical specimen,  $r_g = \sqrt{I/A}$  and  $I = \pi r^4/4$ . Inserting into Equation 4 yields:

$$\sigma_x = \sigma_c \{ 1 \pm (4e_r/r) \sec[(P/EI)^{1/2}(L_e/2)] \}. \quad (5)$$

Equation 5 and Equation 2 are the same except for the secant term. A rough approximation of the secant term will determine if it is significant. For the size B specimen, the length  $L$  of the gage section is approximately 1.3 cm, assuming a fixed-ended column, the effective length  $L_e$  is  $L/2 = 0.64$  cm, and  $r = 0.25$  cm. For a high strength ceramic, the maximum load  $P$  is roughly 110,000 N, and  $E = 410$  GPa. For these values, the secant term is 1.04. This changes the error term in Equation 5 by only 4% of the error and is not significant. Equations 2 and 3 are, therefore, appropriate for the determination of error due to eccentric loading and it is assumed, for further analysis, that the moment due to the lateral movement of the central axis is not significant.

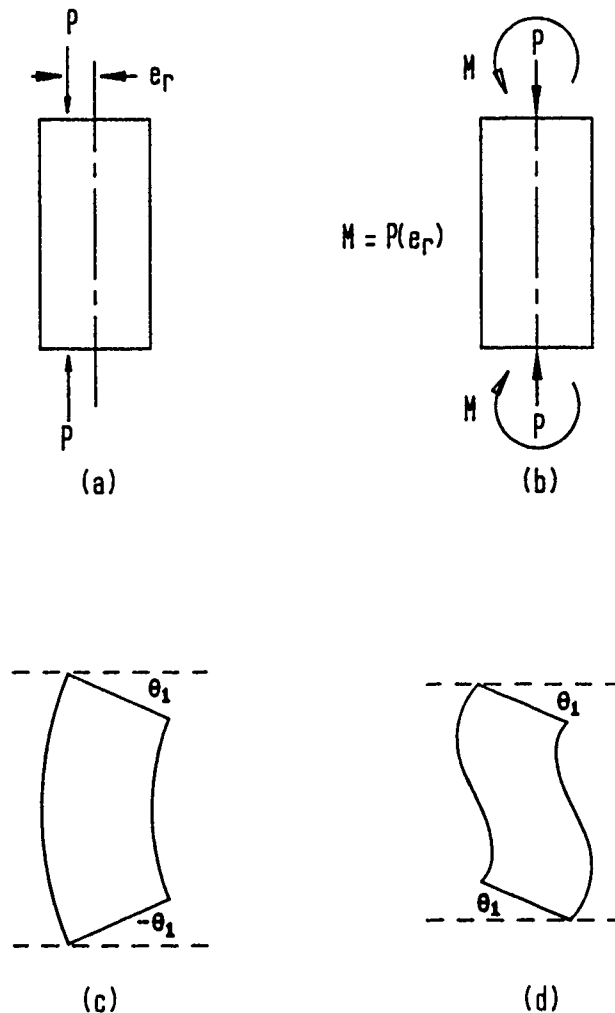


Figure 6. Illustration of specimen showing (a) eccentric loading of idealized compression specimen, (b) the equivalent loading plus applied moment, and (c) and (d) possible idealized specimen configurations if nonparallel loading introduces angular displacement of the end faces.

It is difficult, in practice, to determine the magnitude of  $e_r$  that will occur. The misalignment of the axis of the specimen and the loading block does not necessarily correspond to the effective misalignment of the load, however, assuming that it does, then it is possible to calculate the error that will occur within the framework of the specimen dimension tolerances. For specimen size B, the end-cap diameter is allowed to be  $25 \mu\text{m}$  (0.001 in.) undersize while the load-block diameter can be  $5 \mu\text{m}$  (0.0002 in.) oversize. Half the difference is  $e_r = 15 \mu\text{m}$  (0.0006 in.). Equation 3 gives  $\text{ERR} = -2.3\%$ .

### Nonparallel Surfaces

If any of the loading surfaces, be it the load platforms of the testing machine, the loading blocks, or the specimen itself, are not parallel, the specimen will load eccentrically and bend, forcing the mating surfaces into alignment. The effect is the same as in the previous section where bending was caused by the load being applied off center a distance  $e_r$ . However, in this section, the error will be assumed to be an angle of misalignment  $\theta$  between the mating surfaces of the specimen and the loading blocks.

The first possibility under consideration is that of a specimen forced to assume angle  $\theta_1$  at one end and  $-\theta_1$  at the opposite end (Figure 6c). By symmetry, the applied moments at the ends are equal and opposite. In general, the equation of the elastic curve is given by:<sup>6</sup>

$$\frac{1}{\rho} = d^2y/dx^2 = M(x)/EI \quad (6)$$

where  $\rho$  = the radius of curvature,  $y$  = the lateral displacement of the neutral axis,  $x$  = the longitudinal distance along the specimen, and  $M(x)$  = the moment as a function of  $x$ . For this example,  $M$  is constant and the boundary conditions are (for  $x = 0$ ,  $y = 0$ ) and (for  $x = L$ ,  $y = 0$ ). Integrating Equation 6 twice and using the boundary conditions results in:

$$EIy = Mx^2/2 - MLx/2. \quad (7)$$

Differentiating and noting that for small slopes  $dy/dx = \theta$ :

$$EI\theta = Mx - ML/2. \quad (8)$$

Solving for  $M$  with an angle  $\theta_1$  at  $x = 0$  (and angle  $-\theta_1$  at  $x = L$ ):

$$M = -2EI\theta_1/L. \quad (9)$$

A second possible configuration that the specimen may take if loading surfaces are not parallel is that of a beam with both ends forced to take on the same angle  $\theta_1$  (Figure 6d). By symmetry, the same moment must be applied to each end. However, to balance the moment, an equal and opposite shear force  $F$  is also necessary at each end of the specimen. The applied moment and shear force are related by  $F = 2M/L$  and the moment throughout the specimen is given by  $M(x) = M - Fx = M - 2Mx/L$ . Repeating the same procedure that was used to arrive at Equation 9, and noting that the maximum moment occurs at the ends, yields for this case:

$$M = -6EI\theta_1/L \quad (10)$$

The second configuration, Equation 10, leads to a moment three times that of Equation 9. However, in practice, the moment of Equation 10 may not be realized because the specimen may rotate slightly rather than bending with absolutely fixed ends. A more appropriate value for the bending moment may be intermediate to Equations 9 and 10, and this is:

$$M = -3EI\theta_1/L. \quad (11)$$

The stress due to bending is

$$\sigma_b = 3E\theta_1 r/L \quad (12)$$

and the error on the inside of the bend ( $\sigma_b$  is compressive) is:

$$\text{ERR} = (100)(-3E\theta_1 r)/(\sigma_c L + 3E\theta_1 r). \quad (13)$$

Nonparallel loading is a potentially serious source of error. For a surface with a 1% slope ( $\theta_1 = 0.01$  radians) the error for an average high strength ceramic ( $E = 410$  GPa,  $L = 1.3$  cm,  $r = 0.25$  cm,  $\sigma_c = 5.5$  GPa) is  $\text{ERR} = -31\%$ . The specimen tolerances call for the end faces to be parallel and square to center line with  $5 \mu\text{m}$  (0.0002 in.), which corresponds to an angle  $\theta_1 = 0.001$ . For this angle,  $\text{ERR} = -4.3\%$ .

#### Error Due to Measurement of Diameter of Gage Section

If the measured radius of the gage section is ( $r$ ), and the actual radius is ( $r + e_r$ ), then the error in the stress calculation is given by:

$$\text{ERR} = (100)2e_r/r. \quad (14)$$

Micrometers that read to the  $2 \mu\text{m}$  (0.0001 in.) are roughly accurate to  $6 \mu\text{m}$  (0.0003 in.). This is an  $e_r/r$  ratio of 0.0015 and the error is  $\text{ERR} = 0.3\%$ .

#### Error in the Load Measurement

Error in the load measurement  $e_L$  translates directly to error in the stress calculation:

$$\text{ERR} = (100)e_L/P. \quad (15)$$

Load measurement should be accurate to 1%.

### CONCLUSIONS

Seven materials and two specimen sizes have been successfully tested. Compression strengths approaching 7 GPa (1 million psi) have been measured. A number of results indicate that failure initiates within or immediately adjacent to the gage section, as intended. The standard deviation of the compression strengths is low, which is consistent with the mechanism of compressive failure. The incidence of end-cap failure is not correlated with low strengths, and finite element analysis shows that tensile forces generated in the end caps are probably not sufficient to initiate failure.

FEA also shows that the gage-section stress state is approximately uniaxial, however, there is a stress concentration at the point of tangency where the gage section and fillet meet. The stress at this point is 9% higher than the nominal gage-section stress. It is likely that failure initiates at this point, therefore, the reported strength represents a conservative value.

A fortunate characteristic of compression testing is that almost all likely sources of error will lead to a conservative estimate of strength. The most severe error occurs when the specimen is loaded with nonparallel surfaces and is forced to bend.

Two different sizes of alumina specimens were tested by different investigators 3 years apart. The difference in strength between the two sizes is small considering the number of experimental errors that could come into play. This suggests that the procedure is reproducible and accurate, and is also supporting evidence for the current model of compression failure which implies that compression strength is volume independent.

While the present specimen design is quite good, further finite element work should be done to determine if small modifications to the design could further reduce stress concentrations and tensile stresses.

## APPENDIX A.

The following pages are the design drawings, sizes A and B, for the ceramic test specimens and the matching tungsten carbide loading blocks. For all drawings, the end faces are extremely critical. They should be parallel and square to the center line within 0.0002 in. All diameters should be concentric to within 0.0002 inch. All dimensions are in inches.

The size of the grinding wheel used to make fillet #1 (meets the gage section) must provide a smooth blend to the gage section so that the fillet becomes tangent to the center line directly in line with the outer diameter of the gage section.

The extremely close tolerances called for in these specifications necessitate machining procedures that will produce highly smooth surfaces. Each successive grinding pass should remove the damage layer from the previous grinding pass so that excessive residual stresses and machining microcracks are avoided.

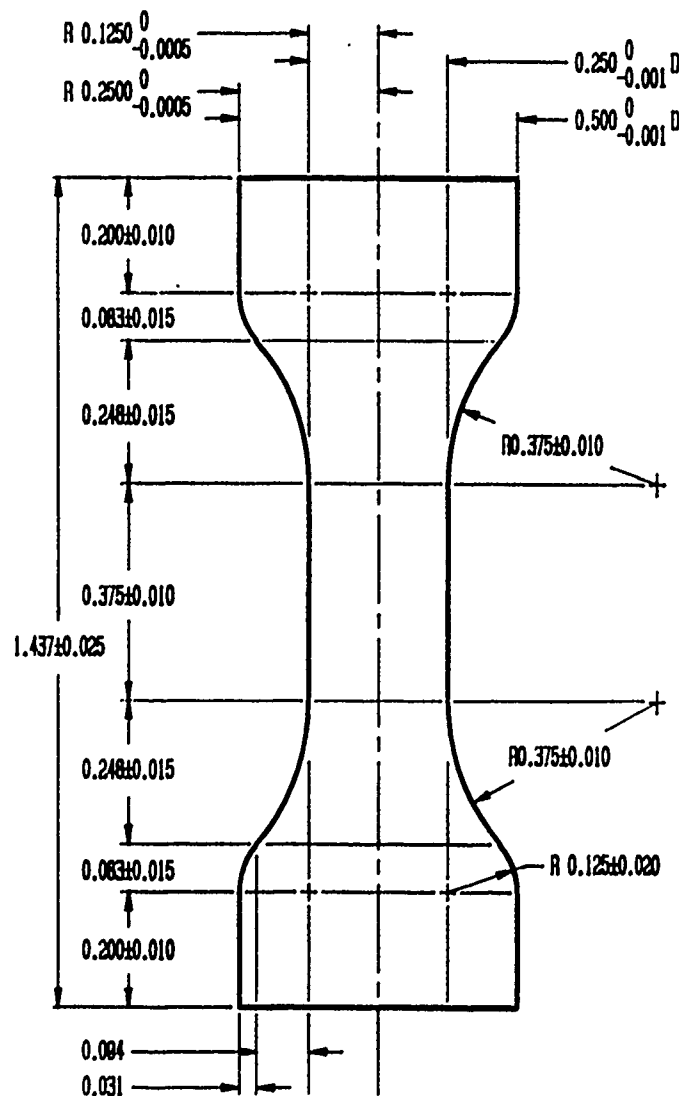


Figure A-1. Compression test specimen size A. Scale: 1 in. = 0.25 in.

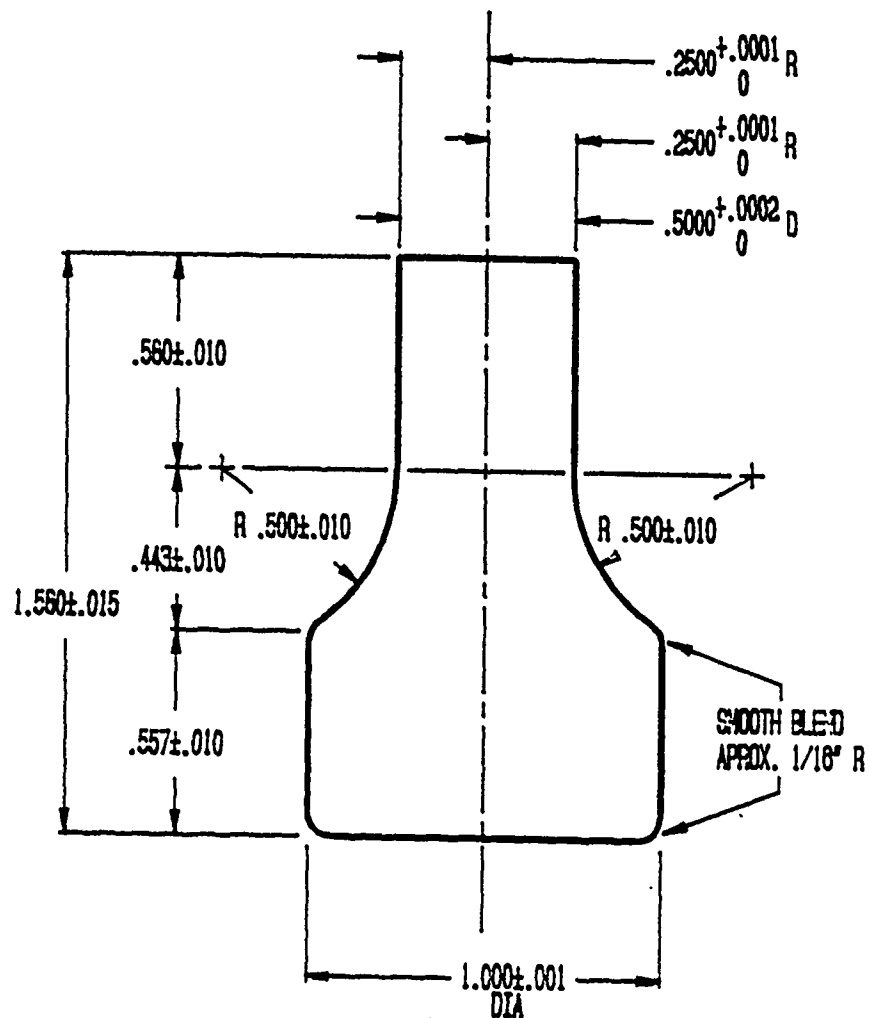


Figure A-2. Load block size A. Scale: 1 in. = 0.5 in.



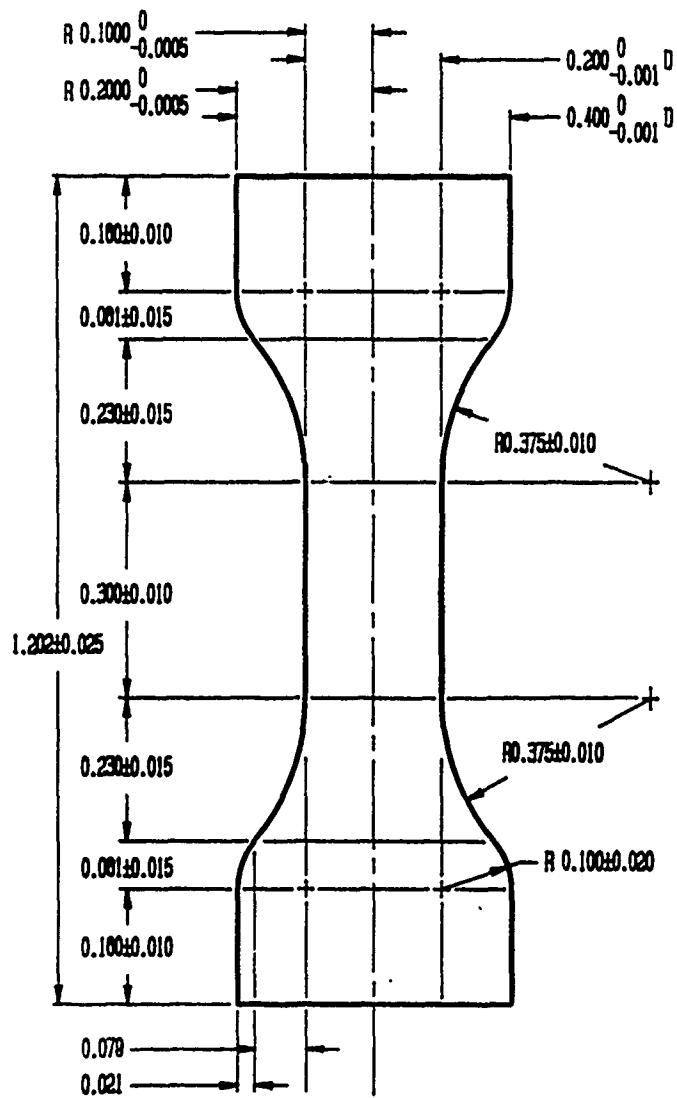


Figure A-3. Compression test specimen size B. Not to scale.



## APPENDIX B.

To determine the validity of the current specimen configuration as a true test of uniaxial compressive strength, a finite element analysis was done to determine the state of stress in the loaded specimen. The FEA was performed using the FORTRAN program ABCDE developed at the U.S. Army Materials Technology Laboratory. The analysis is based on linear elastic, small strain theory simplified by our axisymmetric geometry and axisymmetric quasi-static loading. From this basis, the following relationships are obtained relative to the cylindrical coordinate system  $r, z, \theta$ :

(strain displacement)

$$\epsilon_r = \frac{\partial U_r}{\partial r} \qquad \gamma_{rz} = \frac{\partial U_r}{\partial z} + \frac{\partial U_z}{\partial r}$$

$$\epsilon_\theta = \frac{U_r}{r} \qquad \gamma_{r\theta} = \gamma_{\theta z} = 0$$

$$\epsilon_z = \frac{\partial U_z}{\partial z}$$

(stress strain)

$$\sigma_r = 2\mu \epsilon_r + \lambda(\epsilon_r + \epsilon_\theta + \epsilon_z)$$

$$\sigma_\theta = 2\mu \epsilon_\theta + \lambda(\epsilon_r + \epsilon_\theta + \epsilon_z)$$

$$\sigma_z = 2\mu \epsilon_z + \lambda(\epsilon_r + \epsilon_\theta + \epsilon_z)$$

$$\tau_{rz} = \mu \gamma_{rz} ; \tau_r = \tau_z = 0$$

where the Lamé constants are

$$\mu = \frac{E}{2(1+\nu)} \qquad \lambda = \frac{E\nu}{(1+\nu)(1-2\nu)}$$

and  $E$  = Young's modulus,  $\nu$  = Poisson's ratio,  $\epsilon$  = axial strain,  $\gamma$  = shear strain,  $\sigma$  = axial stress,  $\tau$  = shear stress, and  $U$  is the displacement field.

The test configuration modeled includes the tungsten carbide loading block as well as the test specimen to more accurately depict the specimen's stress field. Specimen size B was chosen for the FEA since most of our testing has been done with this size. The axisymmetric finite element model used is shown in Figure B-1. It is constructed from biquadratic displacement-based isoparametric elements (8-noded quadrilaterals) and contains 4,900 degrees of freedom. Since this problem possesses reflective symmetry about the  $z = 0$  plane, tractions parallel to this plane and displacements perpendicular to this plane were prescribed as zero. A uniform axial displacement was applied to the top boundary of the loading block such that the resultant force applied across the entire surface would create a nominal gage-section stress, in the specimen, equal to the experimentally obtained average strength.

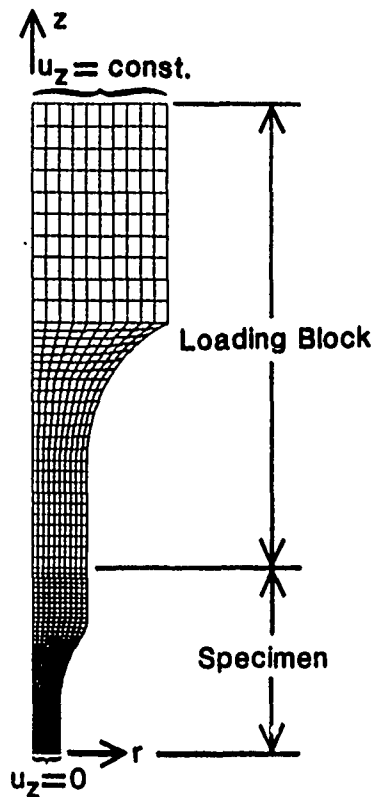


Figure B-1. Axisymmetric finite element model of ceramic compression specimen and loading block with boundary conditions indicated.

Initially, it was unclear whether the specimen/loading block interface would be more accurately modeled as having no friction or infinite friction. Both analyses were done and these showed that (i) the lateral forces generated would not be large enough to cause sliding between the two pieces and (ii) neither assumption has a significant effect on the gage-section stress state or the location and magnitude of the maximum tensile stresses in the specimen end cap. Therefore, the interface was assumed to be one of infinite friction.

All seven materials discussed in the present report were modeled. Because the form of the stress fields and locations of the stress extrema were nearly identical for each material, only the stress contour plots for alumina, which should be representative of any high strength ceramic, are presented here. Figures B-2 through B-7 are contour plots of axial, hoop, radial, and shear stresses as well as two principal stresses  $\sigma_1$  and  $\sigma_3$  which represent the maximum and minimum principal stresses, respectively ( $\sigma_3 < \sigma_2 < \sigma_1$ ).

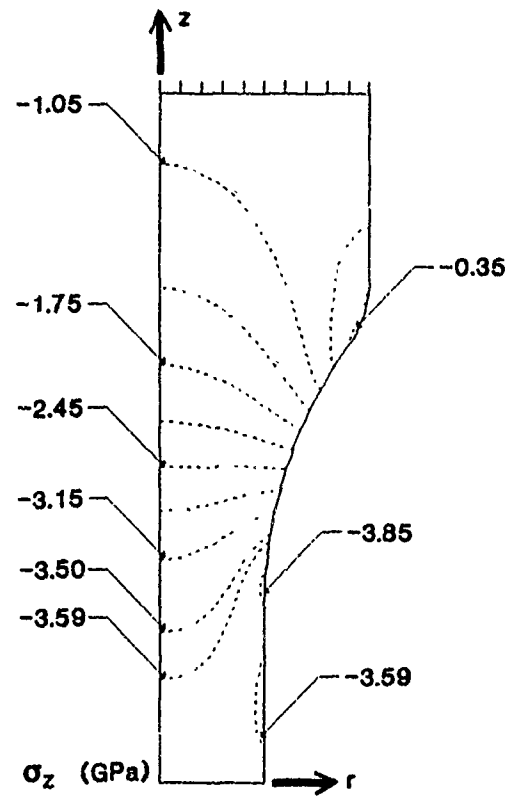


Figure B-2. Contour plot of axial stress  $\sigma_z$  (GPa).

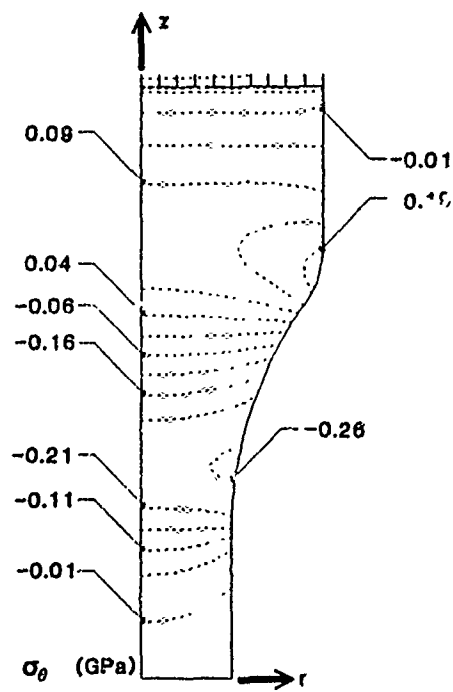


Figure B-3. Contour plot of hoop stress  $\sigma_\theta$  (GPa).

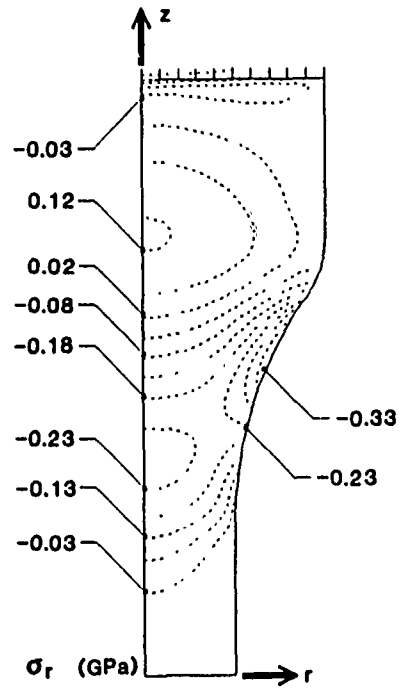


Figure B-4. Contour plot of radial stress  $\sigma_r$  (GPa).

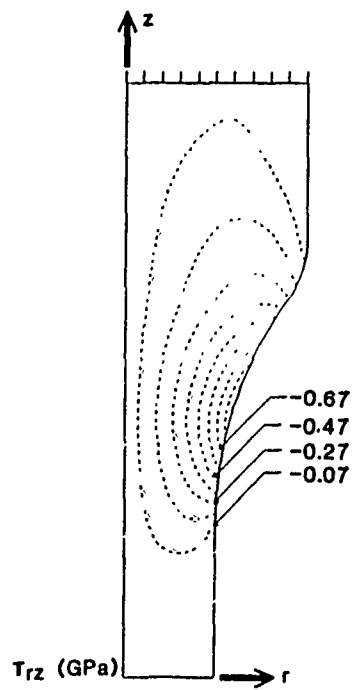


Figure B-5. Contour plot of shear stress  $\tau_{rz}$  (GPa).

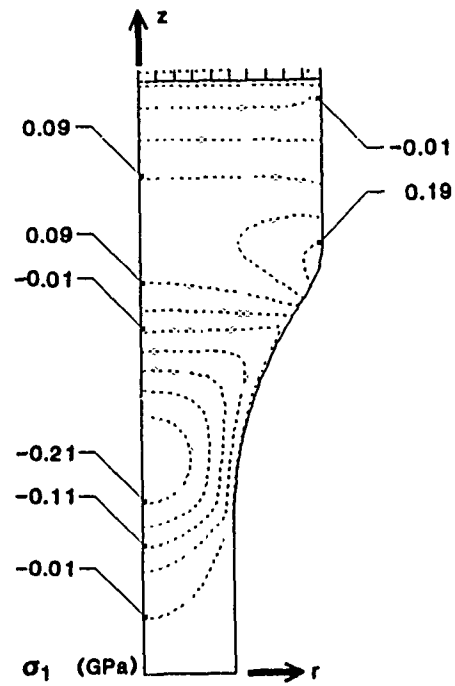


Figure B-6. Contour plot of first principal stress  $\sigma_1$  ( $\sigma_3 < \sigma_2 < \sigma_1$ ).

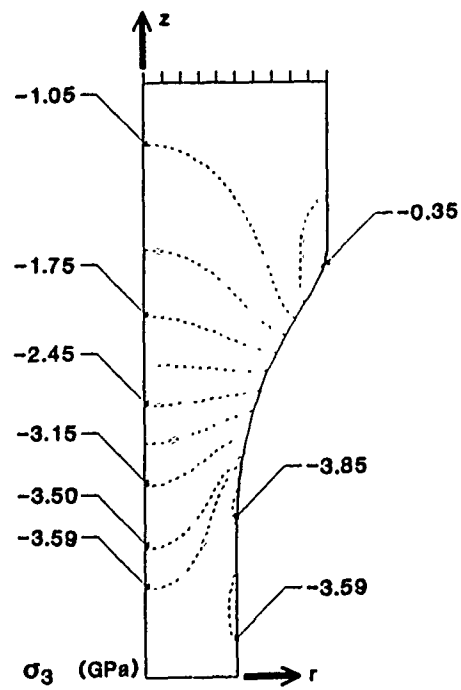


Figure B-7. Contour plot of third principal stress  $\sigma_3$  ( $\sigma_3 < \sigma_2 < \sigma_1$ ).

## DISTRIBUTION LIST

No. of Copies	To	No. of Copies	To
1	Office of the Under Secretary of Defense for Research and Engineering, The Pentagon, Washington, DC 20301	2	Commander, U.S. Army Infantry Board, Fort Benning, GA 31905
1	ATTN: Mr. J. Persh	2	ATTN: Materiel Division
1	Dr. W. E. Snowden		
1	Director, Defense Advanced Research Project Agency, 1400 Wilson Boulevard, Arlington, VA 22901		Commander, U.S. Army Aviation Systems Command, Aviation Research and Technology Activity, Aviation Applied Technology Directorate, Fort Eustis, VA 23604-5577
1	ATTN: LTC P. H. Sullivan	1	ATTN: SAVRT-TY-ASV, Mr. McAllister
1	Dr. J. Richardson	1	SAVRT-TY-ASV, W. Swink
1	Dr. B. Wilcox		
1	LTC D. Wance		Commander, U.S. Army Aviation Systems Command, 4300 Goodfellow Boulevard, St. Louis, MO 6312C-1798
	Commander, U.S. Army Laboratory Command, 2800 Powder Mill Road, Adelphi, MD 20783-1145	1	ATTN: AMSAV-GTD
2	ATTN: AMSLC-DL, Mr. R. Vitali	1	AMSAV-E
1	AMSLC-CT	1	AMCPEO-AV
	Commander, Defense Technical Information Center, Cameron Station, Bldg. 5, 5010 Duke Street, Alexandria, VA 22304-6145		Commander, Rock Island Arsenal, Rock Island, IL 61299-6000
2	ATTN: DTIC-FDAC	1	ATTN: SMCRI-SEM-T
1	Metals and Ceramics Information Center, Battelle Columbus Laboratories, 505 King Avenue, Columbus, OH 43201		Naval Research Laboratory, Washington, DC 20375
	Commander, Army Research Office, P.O. Box 12211, Research Triangle Park, NC 27709-2211	1	ATTN: Dr. G. R. Yoder - Code 6384
1	ATTN: Information Processing Office		Chief of Naval Research, Arlington, VA 22217
1	SLCRO-MD, Dr. I. Ahmad	1	ATTN: Code 471
	Commander, U.S. Army Materiel Command, 5001 Eisenhower Ave. Alexandria, VA 22333		Director, Structural Mechanics Research, Office of Naval Research, 800 North Quincy Street, Arlington, VA 22203
1	ATTN: AMCLD	1	ATTN: Bruce MacDonald
1	AMCDE-SR, Dr. R. Chait	1	Ralph Lud
1	Mr. R. Zigler		Commander, David Taylor Naval Ship Research and Development Center, Bethesda, MD 20084
	Commander, U.S. Army Materiel Systems Analysis Activity, Aberdeen Proving Ground, MD 21005	1	ATTN: Rod Peterson - Code 1240
1	ATTN: AMXSY-MP, H. Cohen	1	Herb Wolk - Code 1740.1
	Commander, U.S. Army Missile Command, Redstone Scientific Information Center, Redstone Arsenal, AL 35898-5241	1	Richard Swanek - Code 1240
1	ATTN: AMSMI-RD-CS-R/Doc		Naval Air Development Center, Warminster, PA 18974
1	AMSMI-RLM	1	ATTN: Code 6062, Irv Shaffer
	Commander, U.S. Armament, Munitions and Chemical Command, Dover, NJ 07801		Naval Air System Command, Department of the Navy, Washington, DC 20360
2	ATTN: Technical Library	1	ATTN: AIR-03PAF
1	AMDAR-LCA, Mr. Harry E. Peibly, Jr., PLASTEC, Director	1	AIR-5164J, LT COL J. Sebolka
	Commander, U.S. Army Natick Research, Development and Engineering Center, Natick, MA 01760	1	SEA-05M, Dr. Alex Kaznoff
1	ATTN: Technical Library	1	SEA-05MB, LCDR W. M. Elger
1	Dr. R. Lewis	1	SEA-05R 25, C. Zanits
	Commander, U.S. Army Tank-Automotive Command, Warren, MI 48397-5000		Naval Material Command, Washington, DC 20360
2	ATTN: AMSTA-TSL, Technical Library	1	ATTN: MAT-0331
1	AMSTA-ZSK		Naval Research Laboratory, 455 Overlook Avenue, Washington, DC 20375
1	AMSTA-RSK, Sam Goodman	1	ATTN: T. W. Crooker
1	AMSTA-RSK, David Tenenbaum		Naval Surface Weapons Center, Dahlgren Laboratory, Dahlgren, VA 22448
1	AMSTA-RSK, Dr. James L. Thompson	1	ATTN: Code G-54, Mr. J. Hall
1	AMCPM-M113-T, G. B. Singh	1	Code R-35, Dr. B. Smith
1	AMCPM-M113, Mr. Joseph Loiselle		Naval Weapons Center, China Lake, CA 93555
1	AMCPM-BFVS, Gary Chamberlain	1	ATTN: Code 40701
	Commander, U.S. Army Materiel Systems Analysis Activity, Aberdeen Proving Ground, MD 21005-5071	1	Code 408
1	ATTN: AMXSY-GI, Gary Holloway		Commander, U.S. Air Force Wright Research & Development Center, Wright-Patterson Air Force Base, OH 45433 6523
	Commander, Combat Systems Test Activity, Aberdeen Proving Ground, MD 21005-5059	1	ATTN: WRDC/MLC
2	ATTN: STECS-AA-R, Roy Falcone	1	WRDC/MLLP, D. M. Forney, Jr.
	Director, U.S. Army Ballistic Research Laboratory, Aberdeen Proving Ground, MD 21005-5066	1	WRDC/MLBC, Mr. Stanley Schulman
1	ATTN: SLCBR-D, Dr. J. Frasier	1	WRDC/FIBA, Mr. L. G. Kelly
1	SLCBR-TB, Dr. W. Kitchens	1	WRDC/FIES, Mr. A. G. Kurtz
1	SLCBR-TB, Mr. Thomas Havel	1	WRDC/FIESD, Mr. A. Kurtz
1	SLCBR-TB, Dr. W. Gillich		National Aeronautics and Space Administration, Marshall Space Flight Center, Huntsville, AL 35812
1	SLCBR-TB, Mr. W. Gooch	1	ATTN: R. J. Schwinghammer, EH01, Dir, M&P Lab
1	SLCBR-TB, Dr. L. Magness	1	Mr. W. A. Wilson, EH41, Bldg 4612
			Aeronautical Systems Division (AFSC), Wright-Patterson Air Force Base, OH 45433-6503
		1	ATTN: ASD/ENFEF, D. C. Wright
		1	ASD/ENFTV, D. J. Wallick
		1	ASD/XRM, G. B. Bennett



No. of Copies	To
	Air Force Armament Laboratory, Eglin Air Force Base, FL 32542
1	ATTN: AFATL/DLYA, V. D. Thornton
1	Mr. W. Dyess
	NASA - Ames Research Center, Army Air Mobility Research and Development Laboratory, Mail Stop 207-5, Moffett Field, CA 94035
1	ATTN: SAVDL-AS-X, F. H. Immen
	U.S. Department of Commerce, National Institute of Standards and Technology, Gaithersburg, MD 20899
1	ATTN: Stephen M. Hsu, Chief, Ceramics Division, Institute for Materials Science and Engineering
	Director, Central Intelligence Agency, P.O. Box 1925, Washington, DC 20505
1	ATTN: OSWR-OSD, Ward Waltman
1	R. Gomez
1	J. Backofen
	U.S. Secret Service, Technical Development and Planning Division, 1301 L Street, N.W., Room 800, Washington, DC 20005
1	ATTN: John McCalla
	Office of Security, Department of State, Washington, DC 20520
1	ATTN: A/SY/OPS/T
	FMC Corporation, Ordnance Engineering Division, 1105 Coleman Avenue, San Jose, CA 95108
1	ATTN: Ron Musante
1	Tony Lee
1	Claude Braafladt
	General Dynamics, Land Systems Division, 38500 Mound Road, Mail Zone 4362029, Sterling Heights, MI 48310
1	ATTN: Mr. Richard Auyer
	United States Steel Corporation, Research Laboratory, Monroeville, PA 15146
1	ATTN: Dr. John M. Barsom
	L. Raymond & Associates, P.O. Box 7925, Newport Beach, CA 92658-7925
1	ATTN: Dr. L. Raymond
	Ingersoll Rand Oilfield Products Division, P.O. Box 1101, Pampa, TX 79065
1	ATTN: Mr. W. L. Hallerberg
	Lukens Steel Company, Coatesville, PA 19320
1	ATTN: Dr. E. G. Hamburg
	LTV Steel Corporation, 410 Oberlin Avenue SW, Massillon, OH 44646
1	ATTN: Mr. R. Sweeney
1	Mr. W. H. Brechtel
1	Mr. B. G. Hughes
	Boeing Advanced Systems, P.O. Box 3707, Seattle, WA 98124-2207
1	ATTN: R. J. Bristow, MS 33-04
1	W. Herlin, MS 33-04
	Sikorsky Aircraft, A Division of United Aircraft Corporation, Main Street, Stratford, CT 06601
1	ATTN: George Karas
	Teledyne CAE, 1330 Laskey Road, Toledo, OH 43697
1	ATTN: Librarian, M. Dowdell
	Fairchild Industries, Inc., Fairchild Republic Company, Conklin Street, Farmingdale, Long Island, NY 11735
1	ATTN: Engineering Library, G. A. Mauter
	Gruman Aerospace Corporation, South Oyster Bay Road, Bethpage, NY 11714
1	ATTN: Technical Information Center, J. Davis

No. of Copies	To
	McDonnell Douglas Helicopter Company, 5000 E. McDowell Road, Mesa, AZ 85205-9797
1	ATTN: Library, 2/T2124, D. K. Goss
1	Mr. A. Hirko
1	Mr. L. Soffa
	IIT Research Institute, 10 West 35th Street, Chicago, IL 60616
1	ATTN: K. McKee
	Kaman Aerospace Corporation, Old Winsor Road, Bloomfield, CT 06002
1	ATTN: H. E. Showalter
	Lockheed-California Company, A Division of Lockheed Aircraft Corporation, Burbank, CA 91503
1	ATTN: Technological Information Center, 84-40, U-35, A-1
	Vought Corporation, P.O. Box 5907, Dallas, TX 75232
1	ATTN: D. M. Reedy, 2-30110
	Martin Marietta Corporation, Orlando Division, P.O. Box 5837, Orlando, FL 32805
1	ATTN: Library, M. C. Griffith
	McDonnell Douglas Corporation, 3855 Lakewood Boulevard, Long Beach, CA 90846
1	ATTN: Technical Library, C1 290/36-84
	Northrop Corporation, Aircraft Division, 3901 W. Broadway, Hawthorne, CA 90250
1	ATTN: Mgr. Library Services, H. W. Jones
	Parker Hannifin Corporation, 14300 Alton Parkway, Irvine, CA 92718
1	ATTN: C. Beneker
	Armament Systems, Inc., 326 W. Katella Ave., 4-K, Orange, CA 92667
1	ATTN: J. Musch
	Beech Aircraft Corporation, 9709 E. Central Avenue, Wichita, KS 67206
1	ATTN: Engineering Library
	Bell Helicopter Company, A Textron Company, P.O. Box 482, Fort Worth, TX 76101
1	ATTN: J. R. Johnson
	Boeing Helicopters, P.O. Box 16858, Philadelphia, PA 19142-0858
1	ATTN: N. Caravassos, M/S P30-27
	Cessna Military, P.O. Box 7704, Wichita, KS 67277-7704
1	ATTN: Wallace
	Los Alamos National Laboratory, Los Alamos, NM 87545
1	ATTN: R. Mah
1	D. Sandstrom
1	W. Blumenthal
1	R. Barks
	Lawrence Livermore National Laboratory, P.O. Box 808, Livermore, CA 94550
1	ATTN: C. Cline
1	R. Landingham
	Aluminum Company of America, Alcoa Technical Center, Alcoa Center, PA 15069
1	ATTN: A. Becker
	CERCOM, Inc., 1960 Watson Way, Vista, CA 92083
1	ATTN: R. Palicka
	Ceradyne, Inc., 3169 Redhill, Costa Mesa, CA 92626
1	ATTN: E. Conabee
	Morton Co., 1 New Bond Street, Worcester, MA 01606
1	ATTN: R. Bart
	Coors Ceramics Co., 600 Ninth Street, Golden, CO 80401
1	ATTN: R. Paricio

No. of Copies	To
1	Carborundum Co., P.O. Box 1054, Niagara Falls, NY 14302
1	ATTN: J. Hinton
1	R. Palia
	Southwest Research Institute, 6220 Culebra Rd.,
	San Antonio, TX 78248
1	ATTN: C. Anderson
	University of California-San Diego, Dept. of Applied
	Mechanics & Engineering Sciences, La Jolla, CA 92093
1	ATTN: M. Meyers
	Dow Chemical Co., 1776 Building, Midland, MI 48674
1	ATTN: A. Hart
	Lanxide Corp., Tralee Industrial Park, Newark, DE 19711
1	ATTN: M. Newkirk
	General Sciences, Inc , 655 Gravers Road, Plymouth Meeting,
	PA 19462
1	ATTN: P. Zavitsanos

No. of Copies	To
	University of Dayton Research Institute, 300 College Park,
	Dayton, OH 45469
1	ATTN: S. Bless
1	N. Hecht
	SRI International, 333 Ravenswood Ave., Menlo Park,
	CA 94025
1	ATTN: D. Shockey
1	D. Curren
	Director, U.S. Army Materials Technology Laboratory,
	Watertown, MA 02172-0001
2	ATTN: SLCMT-TML, Library
3	Authors

<p>U.S. Army Materials Technology Laboratory Watertown, Massachusetts 02172-0001 A PROPOSED UNIAXIAL COMPRESSION TEST FOR HIGH STRENGTH CERAMICS - William A. Dunlay, Carl A. Tracy, and Paul J. Perrone</p> <p>Technical Report MTL TR 89-89, September 1989, 29 pp- illus-tables, D/A Project: 1L1612105.H84</p> <p>Compressive strength is critical to the performance of ceramics in armor, machine tool bits, and compressively loaded structural components. Traditional compression tests yield misleadingly low values for high strength ceramics. A new test, utilizing a dumb-bell-shaped specimen, has been developed and has successfully measured the strength of Al<sub>2</sub>O<sub>3</sub>, B<sub>4</sub>C, TiB<sub>2</sub>, and SiC. Compression strengths approaching 7 GPa (1 million psi) were measured. Results were accurate, reproducible, and consistent with present compressive fracture theory. A finite element analysis (FEA) was done to confirm a uniaxial stress state. An error analysis examines the severity of procedural errors. The test is simple and cost effective to perform.</p>	<p>AD <u>UNCLASSIFIED</u> UNLIMITED DISTRIBUTION</p> <p>Key Words</p> <p>Advanced ceramics Compression testing Finite element analysis</p>
<p>U.S. Army Materials Technology Laboratory Watertown, Massachusetts 02172-0001 A PROPOSED UNIAXIAL COMPRESSION TEST FOR HIGH STRENGTH CERAMICS - William A. Dunlay, Carl A. Tracy, and Paul J. Perrone</p> <p>Technical Report MTL TR 89-89, September 1989, 29 pp- illus-tables, D/A Project: 1L1612105.H84</p> <p>Compressive strength is critical to the performance of ceramics in armor, machine tool bits, and compressively loaded structural components. Traditional compression tests yield misleadingly low values for high strength ceramics. A new test, utilizing a dumb-bell-shaped specimen, has been developed and has successfully measured the strength of Al<sub>2</sub>O<sub>3</sub>, B<sub>4</sub>C, TiB<sub>2</sub>, and SiC. Compression strengths approaching 7 GPa (1 million psi) were measured. Results were accurate, reproducible, and consistent with present compressive fracture theory. A finite element analysis (FEA) was done to confirm a uniaxial stress state. An error analysis examines the severity of procedural errors. The test is simple and cost effective to perform.</p>	<p>AD <u>UNCLASSIFIED</u> UNLIMITED DISTRIBUTION</p> <p>Key Words</p> <p>Advanced ceramics Compression testing Finite element analysis</p>

<p>U.S. Army Materials Technology Laboratory Watertown, Massachusetts 02172-0001 A PROPOSED UNIAXIAL COMPRESSION TEST FOR HIGH STRENGTH CERAMICS - William A. Dunlay, Carl A. Tracy, and Paul J. Perrone</p> <p>Technical Report MTL TR 89-89, September 1989, 29 pp- illus-tables, D/A Project: 1L1612105.H84</p> <p>Compressive strength is critical to the performance of ceramics in armor, machine tool bits, and compressively loaded structural components. Traditional compression tests yield misleadingly low values for high strength ceramics. A new test, utilizing a dumb-bell-shaped specimen, has been developed and has successfully measured the strength of Al<sub>2</sub>O<sub>3</sub>, B<sub>4</sub>C, TiB<sub>2</sub>, and SiC. Compression strengths approaching 7 GPa (1 million psi) were measured. Results were accurate, reproducible, and consistent with present compressive fracture theory. A finite element analysis (FEA) was done to confirm a uniaxial stress state. An error analysis examines the severity of procedural errors. The test is simple and cost effective to perform.</p>	<p>AD <u>UNCLASSIFIED</u> UNLIMITED DISTRIBUTION</p> <p>Key Words</p> <p>Advanced ceramics Compression testing Finite element analysis</p>
<p>U.S. Army Materials Technology Laboratory Watertown, Massachusetts 02172-0001 A PROPOSED UNIAXIAL COMPRESSION TEST FOR HIGH STRENGTH CERAMICS - William A. Dunlay, Carl A. Tracy, and Paul J. Perrone</p> <p>Technical Report MTL TR 89-89, September 1989, 29 pp- illus-tables, D/A Project: 1L1612105.H84</p> <p>Compressive strength is critical to the performance of ceramics in armor, machine tool bits, and compressively loaded structural components. Traditional compression tests yield misleadingly low values for high strength ceramics. A new test, utilizing a dumb-bell-shaped specimen, has been developed and has successfully measured the strength of Al<sub>2</sub>O<sub>3</sub>, B<sub>4</sub>C, TiB<sub>2</sub>, and SiC. Compression strengths approaching 7 GPa (1 million psi) were measured. Results were accurate, reproducible, and consistent with present compressive fracture theory. A finite element analysis (FEA) was done to confirm a uniaxial stress state. An error analysis examines the severity of procedural errors. The test is simple and cost effective to perform.</p>	<p>AD <u>UNCLASSIFIED</u> UNLIMITED DISTRIBUTION</p> <p>Key Words</p> <p>Advanced ceramics Compression testing Finite element analysis</p>